nature physics

SUPPLEMENTARY INFORMATION

DOI: 10.1038/NPHYS3342

One minute parity lifetime of a NbTiN Cooper-pair transistor

David J. van Woerkom,* Attila Geresdi*,† and Leo P. Kouwenhoven

QuTech and Kavli Institute of Nanoscience,

Delft University of Technology, 2600 GA Delft, The Netherlands.

* These authors contributed equally to this work.

† Corresponding author, e-mail address: a.geresdi@tudelft.nl

DOI: 10.1038/NPHYS3342

DEVICE FABRICATION

device	island size (nm × nm)	junction size (nm × nm)	NbTiN thickness (nm)	traps	oxygen exposure (Torr×s)	R_N (kΩ)
N	500 × 500	200 × 200	70	no	7400	58
S1	450 × 200	200 × 200	100	yes	150	125
S2	450 × 250	200 × 250	100	yes	150	66

TABLE S1. **Device fabrication parameters of the CPTs discussed in the main text.**

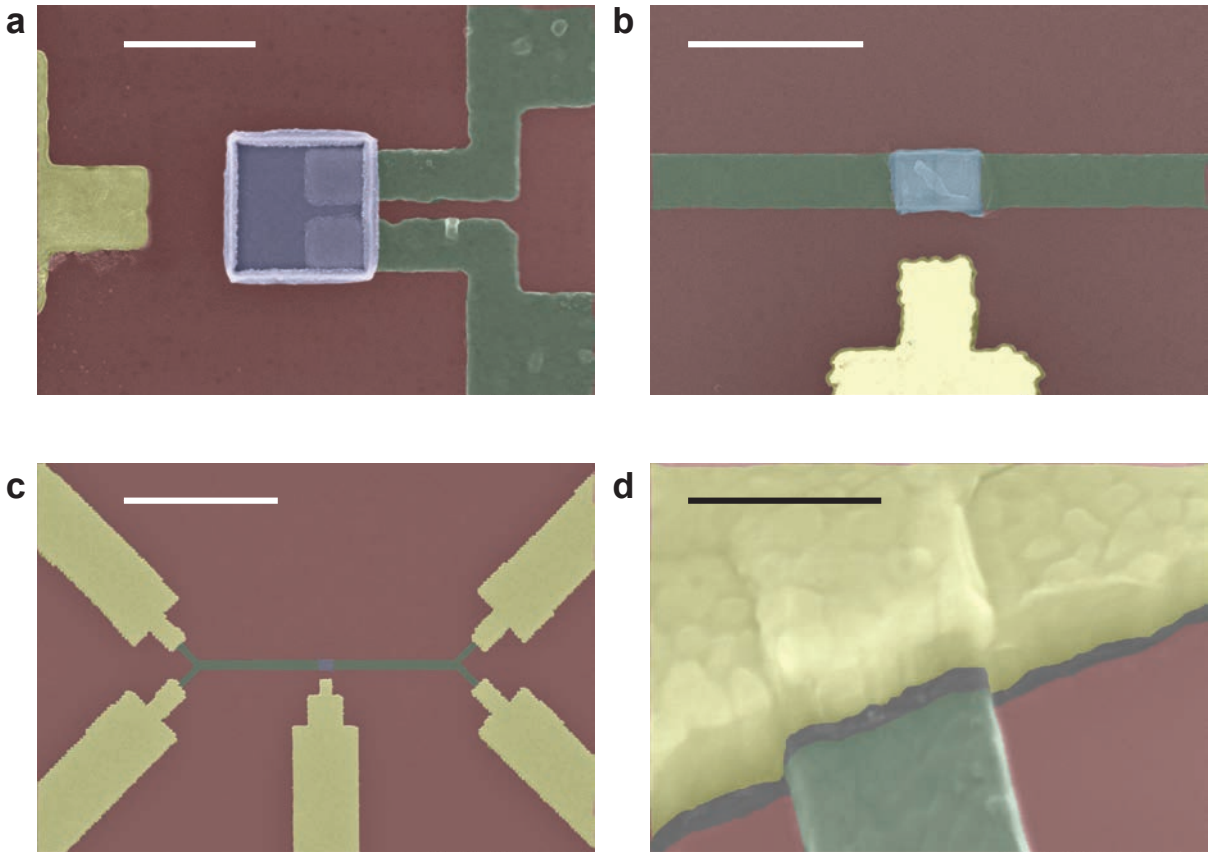

FIG. S1. **Scanning electron microscope images of the CPTs.** **(a)** Non-shielded device N without quasiparticle traps. **(b), (c), (d)** Shielded device S2 featuring quasiparticle traps. Colour legend: dark red: Si/SiO_2 substrate; light blue: NbTiN island, green: aluminium leads and yellow: normal metal (Ti/Au) gate and quasiparticle traps. Scale bars denote 500 nm **(a)**, 1000 nm **(b)**, 5 μm **(c)** and 200 nm **(d)**, respectively.

MEASUREMENT SETUP

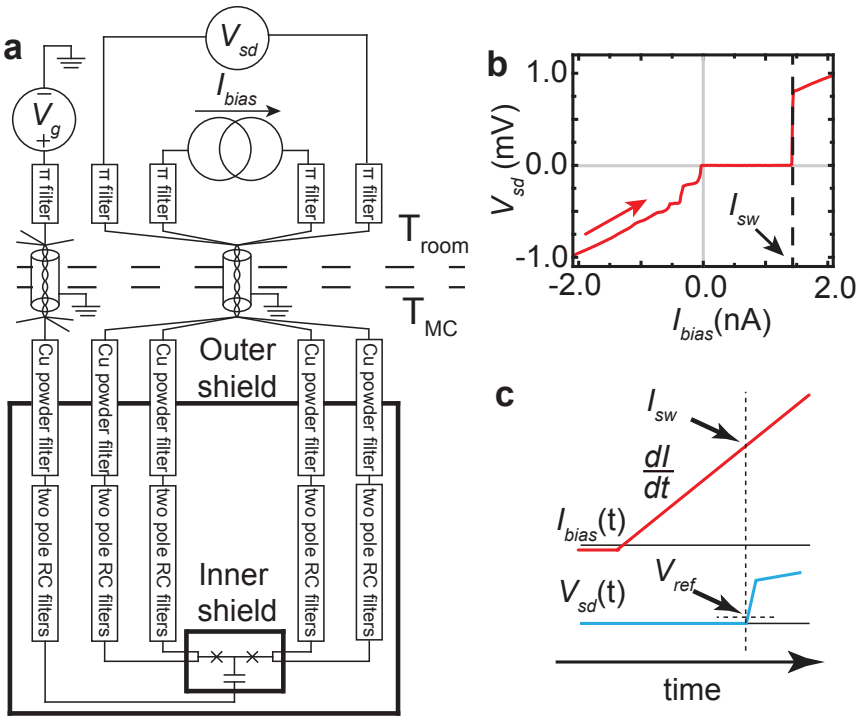

FIG. S2. **Measurement electronic setup and typical waveforms.** (a) Schematics of the measurement. (b) Typical experimental $V-I$ trace exhibiting a well-defined switching current, $I_{\rm sw}$. We observe a retrapping current $I_r \ll I_{\rm sw}$ characteristic to unshunted Josephson junctions in the low temperature limit [37]. The additional features in the resistive state are consistent with Fiske steps [38]. (c) Current ramp (red) with a slope of dI/dt probing $I_{\rm sw}$ which is recorded when the measured $V_{\rm sd}$ (blue) reaches $V_{ref} \sim 10\,\mu$V.

BASIC CHARACTERIZATION OF THE CPT

It is important to note that we find a finite subgap conductance at $eV_{\rm sd} < 2\Delta_{\rm NbTiN}$ which is consistent with the presence of the subgap quasiparticle states justifying the analysis leading to equation (1) in the main text. Furthermore, we observe reduced $\Delta_{\rm NbTiN} < 1.4\,$meV values compared to that of bulk films ($\Delta > 2\,$meV) [39], which we attribute to the chemical interaction between the AlO_x tunnel barrier and the NbTiN film. Indeed, it was shown earlier that the critical temperature of Nb films is particularly very sensitive to contamination with

DOI: 10.1038/NPHYS3342

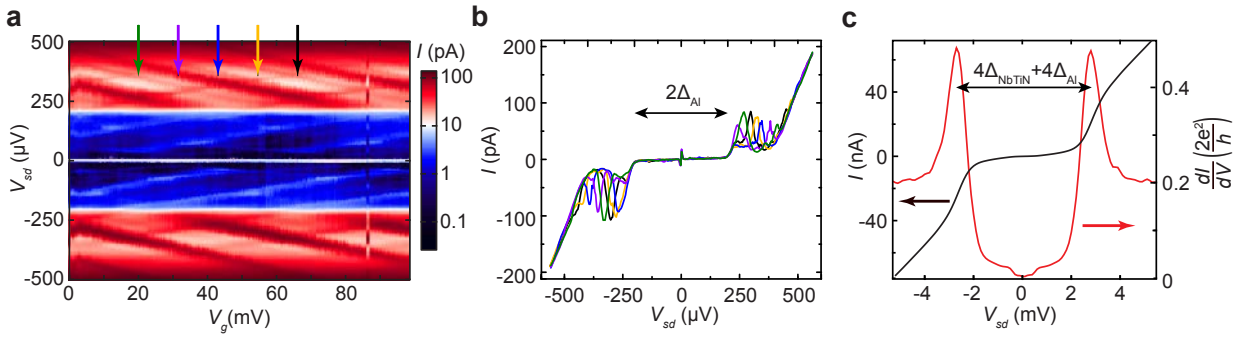

FIG. S3. **Basic characterization of the CPT. (a)** Stability diagram: $\log|I|$ as a function of $V_{\rm sd}$ and V_g of device S1. We estimate E_c based on the resonant Andreev processes (see text). **b** Linecut $I-V$ traces at V_g values depicted by arrows in (a). Characteristic resonant tunneling processes occur in the bias voltage range of $eV_{\rm sd} = \Delta_{\rm Al} \ldots 2\Delta_{\rm Al}$. **(c)** $I-V$ (black) and dI/dV (red) line traces of device S2. Quasiparticle transport is enhanced above a bias voltage of $eV_{\rm sd} = 2(\Delta_{\rm NbTiN} + \Delta_{\rm Al})$.

device	$\Delta_{\rm Al}$ (μeV)	$\Delta_{\rm NbTiN}$ (μeV)	R_N (kΩ)	E_J (μeV)	E_c (μeV)	E_J/E_c calc.	E_J/E_c I_{sw}
N	210	1390	58	54	50	1.08	1.25
S1	218	810	125	17	62	0.28	0.32
S2	220	1300	66	48	49	0.98	1.16

TABLE S2. **Device transport parameters.**

oxygen [40, 41]. However, the nitridized NbTiN compound is presumably less prone to oxidization [42].

EVALUATION OF THE PARITY LIFETIME

We checked the robustness of the extracted parity lifetime against changing the current ramp rate. Typical datasets are shown in Fig. S4, giving $\tau_p = 1.2\,$ms and $\tau_p = 0.98\,$ms for $dI/dt = 100\,$nA/s (red) and $dI/dt = 400\,$nA/s (black), respectively. We estimate the typical uncertainty to be 25%, concluding that τ_p does not depend on dI/dt which validates the analysis in the main text. However, we do not discuss here the intrinsic peak shapes of the bimodal switching current histogram. Since fast gate charge noise influences the measured distribution [43], we cannot distinguish between thermally activated [44] and macroscopic

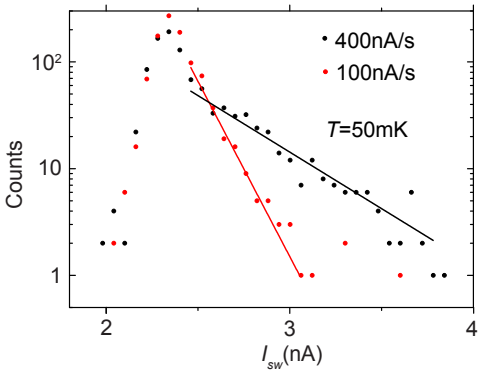

FIG. S4. **Measured switching current histograms at different dI/dt ramp rates.** Colour legend: red: $dI/dt = 100\,\mathrm{nA/s}$, black: $dI/dt = 400\,\mathrm{nA/s}$. The data was acquired on a CPT similar to device N.

quantum tunneling behaviour [37, 45].

We now turn to the temperature dependence of τ_p. In order to get equation (1) in the main text, we assume the following:

i) The superconducting gap of the island ($\Delta_{\mathrm{NbTiN}} \gtrsim 1.3\,\mathrm{meV}$) is much higher than the effective thermal energy describing the quasiparticle population and the gap of the leads ($\Delta_{\mathrm{Al}} \approx 200\,\mu\mathrm{eV}$).

ii) The density of states in the leads is BCS-type: $\rho_{\mathrm{lead}}(E) = \rho_{\mathrm{Al}} \times |E|/\sqrt{E^2 - \Delta_{\mathrm{Al}}^2}$ for $|E| > \Delta_{\mathrm{Al}}$ and zero otherwise.

iii) There is a constant, finite subgap density of states ρ_{subgap} for energies below Δ_{NbTiN} in the island.

iv) the energy dependence of the single electron tunnel probability is negligible over the energy range of $\sim \Delta_{\mathrm{NbTiN}}$, meaning that the tunnel barrier is much higher than Δ_{NbTiN}.

v) The tunnel barriers are identical, each characterized by half the normal state resistance of the full device, R_N.

Considering only single electron tunneling and zero voltage bias across the tunnel barriers, following [46], we get the quasiparticle tunnel rate:

$$\tau_p^{-1} = \frac{2}{e^2(R_N/2)\rho_{\mathrm{Al}}} \frac{\rho_{\mathrm{subgap}}}{\rho_{\mathrm{NbTiN}}} \int_0^\infty \rho_{\mathrm{lead}}(E) f(T,E) dE = \frac{2n_{\mathrm{qp}}}{e^2 R_N \rho_{\mathrm{Al}}} \frac{\rho_{\mathrm{subgap}}}{\rho_{\mathrm{NbTiN}}}. \qquad \text{(S1)}$$

DOI: 10.1038/NPHYS3342

Assigning an effective temperature to the quasiparticle population in the leads, we find:

$$n_{\mathrm{qp}}(T) = 2\int_0^\infty \rho_{\mathrm{lead}}(E) f(T,E) dE = \rho_{\Al}\sqrt{2\pi k_B T \Delta_{\Al}} e^{-\frac{\Delta_{\Al}}{k_B T}} \tag{S2}$$

in the limit of $k_B T \ll \Delta_{\Al}$. For temperatures exceeding 100 mK, we assume that the quasiparticle population is in thermal equilibrium, and therefore the lattice temperature is equivalent to the effective quasiparticle temperature: $\tau_p^{-1}(T) \propto \sqrt{T}\exp(-\Delta_{\Al}/k_B T)$.

We verify this picture by fitting the observed parity lifetimes with $\Delta_{\Al}$ as a free parameter, and find values ranging $170 \ldots 210\,\mu$eV for different devices in good correspondence with the gap determined by voltage bias spectroscopy ($\Delta_{\Al}$ in Table S2).

Notably, the ratio $\rho_{\mathrm{subgap}}/\rho_{\mathrm{NbTiN}}$ is the Dynes parameter [47] of the island material, characterized to be $\lesssim 10^{-3}$ based on measurements of highly resistive single junctions (Fig. S5). With this value and using $\rho_{\Al} = 1.45 \times 10^{47}\,\mathrm{J^{-1}m^{-3}}$ [46], we get $n_{\mathrm{qp}} \sim 3\,\mu\mathrm{m}^{-3}$ for device N based on the observed parity lifetime of 9.5 ms in the low temperature limit.

We now comment on the observed $\Delta^\star \approx 20\,\mu$eV activation energy observed for devices S1 and S2. We estimate the maximal even-odd energy difference to be $\delta E \approx 20 \ldots 30\,\mu$eV based on $E_J \approx E_c \approx 50\,\mu$eV [48] which is in range of the experimentally observed $\Delta^\star$. Similar, activated behaviour of the parity lifetime scaling as $\sim \exp(\delta E/k_B T)$ was reported earlier [49].

Providing another possible explanation, we note that a grain size of ≈ 50 nm can lead to a level spacing of the order of $10\,\mu$eV which can influence single electron transport and hence τ_p if the grains are weakly coupled, i. e. for disordered superconducting films [50]. Disorder-induced fluctuations may also explain the broadening of the coherence peaks (Fig. S3c) [51, 52].

MEASUREMENT OF THE DYNES PARAMETER OF THE NBTIN ISLAND

We estimate the Dynes parameter in equation (1) of the main text by evaluating the subgap conductance of a single NbTiN/AlO_x/Al tunnel junction, where higher order tunneling, i.e. Andreev reflection is strongly suppressed. Based on the measurement data in Fig. S5, we estimate the Dynes parameter to be $\lesssim 10^{-3}$.

We can get an independent estimate of the Dynes parameter by combining eq. (S1) and

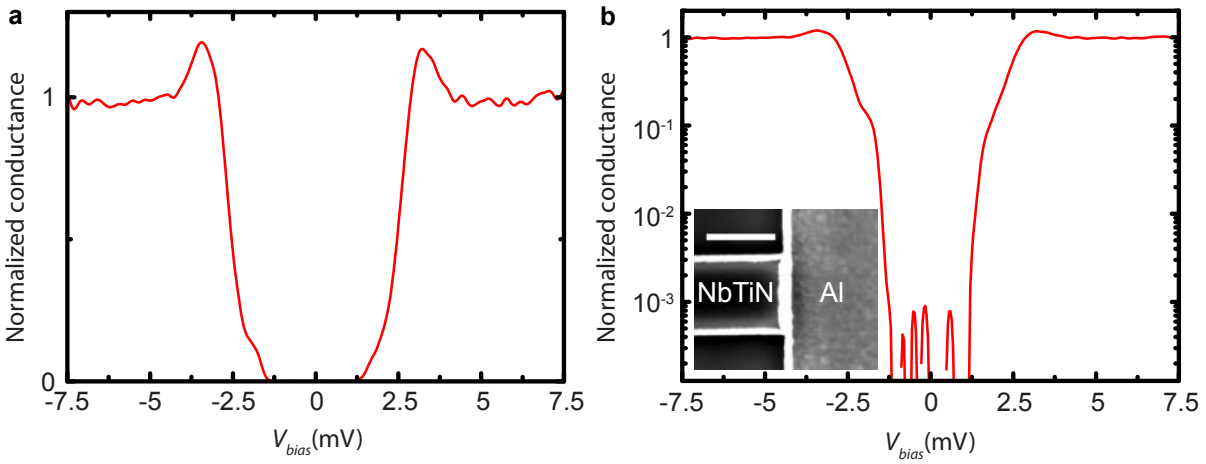

FIG. S5. dI/dV characteristics of a single NbTiN/AlO_x/Al tunnel junction with a normal state resistance of $R_N = 2.4\,\mathrm{M\Omega}$ on the linear **(a)** and on the logarithmic scale **(b)**, respectively. The measurement was performed at $T = 300\,\mathrm{mK}$. The inset in (b) shows the scanning electron microscope image of the device. The scale bar denotes 500 nm.

eq. (S2):

$$\tau_p^{-1} = \frac{2\sqrt{2\pi k_B T \Delta_{\mathrm{Al}}}}{e^2 R_N} \frac{\rho_{\mathrm{subgap}}}{\rho_{\mathrm{NbTiN}}} e^{-\frac{\Delta_{\mathrm{Al}}}{k_B T}}. \tag{S3}$$

We fit the high temperature part of $\tau_p(T)$ shown in Fig. 2c with the functional form of $\tau_p(T) = \frac{A}{\sqrt{T}} e^{\frac{\Delta_{\mathrm{Al}}}{k_B T}}$ where the prefactor A contains the Dynes parameter in addition to known parameters of the device. However, the uncertainty of the fitting makes an order of magnitude estimate possible, and we conclude $\frac{\rho_{\mathrm{subgap}}}{\rho_{\mathrm{NbTiN}}} \sim 10^{-2}$ for all devices which is consistent with the previous estimate.

SUPERCONDUCTING THIN FILM CHARACTERIZATION AND MAGNETIC FIELD DEPENDENCE

Next, we consider the properties of superconducting stripes with layer thickness d, and a width w to find the London penetration depth λ_L and the coherence length ξ. We characterize the upper critical field in the parallel ($B_{c\parallel}$) and perpendicular geometry ($B_{c\perp}$) based on the dI/dV traces of the tunnel junctions of the CPT. In addition, we measure the normal state resistivity of the films that gives an estimate for the mean free path, l_m [53].

First, we establish the length scales of the island material, NbTiN. We find films super-

DOI: 10.1038/NPHYS3342

conducting at $B_\perp = 9\,\mathrm{T}$ which leads to an upper limit of $\xi_{\mathrm{NbTiN}} < 6\,\mathrm{nm}$ following [54]:

$$B_{c\perp} = \frac{\Phi_0}{2\pi\xi^2}. \tag{S4}$$

The penetration depth can be estimated using the normal state resistivity of $\rho = 98\,\mu\Omega\mathrm{cm}$ and the critical temperature of $T = 14.1\,\mathrm{K}$ using the following semi-empirical formula [39]:

$$\lambda_{\mathrm{NbTiN}} = \sqrt{\frac{\rho[\mu\Omega\mathrm{cm}]}{T_c[K]}} \times 105\,\mathrm{nm} \approx 280\,\mathrm{nm}. \tag{S5}$$

Next we estimate length scales of the Al leads based on the electronic transport through the CPT. Typical thin Al films are type-II superconductors in the dirty limit ($l_m < \xi_0$) with a reduced coherence length of $\xi \approx 0.85\sqrt{\xi_0 l_m}$ and with a London penetration depth of $\lambda \approx \lambda_0\sqrt{\xi_0/l_m}$, where $\xi_0 \approx 1500\,\mathrm{nm}$ and $\lambda_0 \approx 16\,\mathrm{nm}$ are the bulk values [54]. For our films, we estimate $l_m \approx 8.5\,\mathrm{nm}$ based on the resistivity of $\rho = 4.3\,\mu\Omega\mathrm{cm}$ [53]. From the stability diagram of the devices, we extract upper critical fields of $B_{c2,\perp} = 36.4 \pm 4\,\mathrm{mT}$ (Fig. S6c) and $B_{c2,\parallel} = 320 \pm 10\,\mathrm{mT}$ (Fig. S6b) leading to a coherence length of $\xi_{\mathrm{Al}} = 96\,\mathrm{nm}$ and $\lambda_{\mathrm{Al}} = 230\,\mathrm{nm}$ which enables vortex formation in the aluminium leads in perpendicular magnetic field.

It is important to observe that $\xi_{\mathrm{NbTiN}} \ll d \approx 100\,\mathrm{nm}$ enables vortex formation for an *in-plane* geometry in the NbTiN island. We find a characteristic suppression of τ_p at $B_\parallel = 70\,\mathrm{mT}$ for device S2 (orange dots in Fig. S6a) and at $B_\parallel = 110\,\mathrm{mT}$ for device S1 (cyan dots in Fig. S6a). Considering the effective cross-sectional areas (see Table S1 for dimensions), we find $\Phi \approx 1.5\Phi_0$ and $\Phi \approx 1.1\Phi_0$ for S2 and S1, respectively, which is in qualitative agreement with the threshold of a single vortex formation in a mesoscopic island [55–57]. We also note that $B_{c2,\parallel}$ of the leads (Fig. S6b) does not depend on the direction of $B_\parallel$, therefore the different evolution of τ_p can only be explained by the different alignment of $B_\parallel$ with respect to the NbTiN islands.

We also note the decrease of switching currents of the upper branch on the same magnetic field scale (Fig. S6c). This is consistent with a Fraunhofer-like interference arising from the current path through the junctions being perpendicular to the applied magnetic field. A clear evaluation of the parity lifetime is possible as long as $\langle I_{\mathrm{sw,u}}\rangle > \langle I_{\mathrm{sw,l}}\rangle$, which in our geometry leads to the same magnetic field range as that of the vortex formation discussed above. However, we did not recover subsequent lobes in higher $B_\parallel$ which is characteristic for Fraunhofer interference.

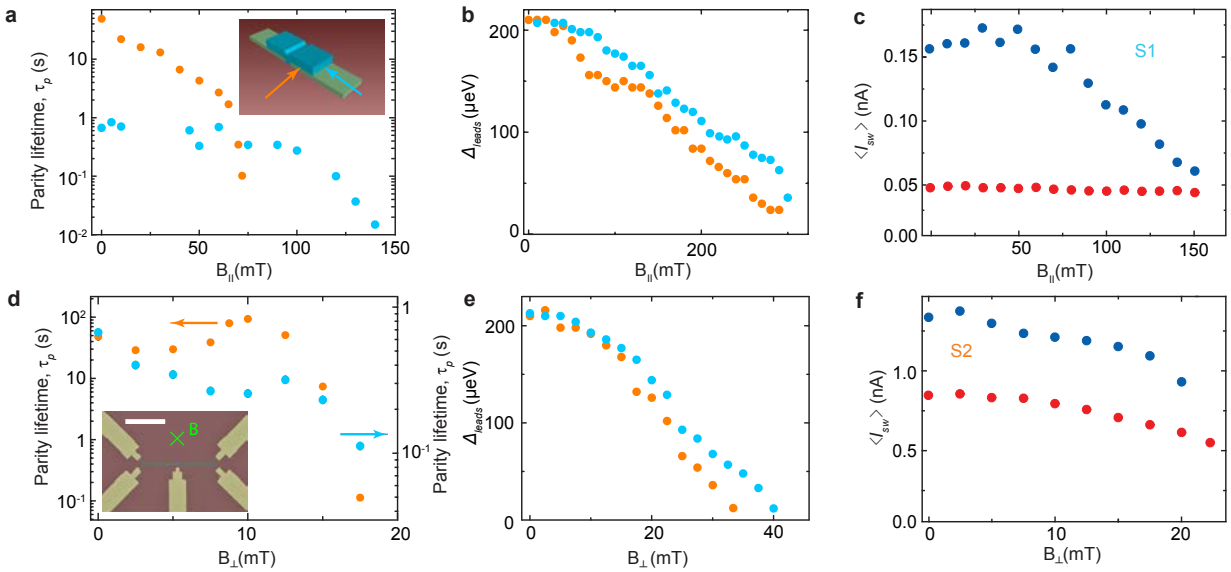

FIG. S6. **Supplementary data on magnetic field dependence of the CPT. (a), (b)** Measured parity lifetime and superconducting gap of the leads as a function of in-plane magnetic field. The inset of panel (a) shows the relative orientation of the field for the two devices. **(c)** The expectation value of the switching current of the lower and upper branch, respectively in the *fast* limit as a function of the magnetic field for device S1. **(d), (e)** The parity lifetime and the superconducting gap as a function of the perpendicular magnetic field. The inset of panel (d) shows the electron microscopy image of the device. The scale bar denotes 5 μm. **(f)** The expectation value of the switching current of the lower and upper branch, respectively in the *fast* limit as a function of the magnetic field for device S2. All measurements were performed at $T = 12$ mK. Colour legend for panels (a), (b), (d) and (e): cyan: device S1; orange: device S2. Colour legend for panels (c) and (f): blue: upper branch, red: lower branch.

In a perpendicular geometry, the vortex phase is stable in a thin stripe above the magnetic field

$$B_{c1,\perp}(w) = \alpha \frac{\Phi_0}{w^2}, \tag{S6}$$

where α is a model-dependent prefactor [58–60] of the order of unity. We reproducibly find the same non-monotonic behaviour of τ_p for devices S1 and S2 with the maximum at $B_\perp \approx 10 \ldots 13$ mT (Fig. S6d), which is in range of $B_{c1,\perp}(w)$ for $w = 200 \ldots 250$ nm, the width of the Al leads near the island. However, both the superconducting gap of the leads (Fig. S6e) and the switching current values (Fig. S6f) decrease monotonously.

DOI: 10.1038/NPHYS3342

[37] D. Massarotti, L. Longobardi, L. Galletti, D. Stornaiuolo, D. Montemurro, G. Pepe, G. Rotoli, A. Barone, and F. Tafuri, Escape dynamics in moderately damped Josephson junctions (review article), *Low Temperature Physics* **38**, 263–272 (2012).

[38] D. Coon and M. Fiske, Josephson AC and step structure in the supercurrent tunneling characteristic, *Phys. Rev.* **138**, A744–A746 (1965).

[39] T. Matsunaga, H. Maezawa, and Takashi Noguchi, Characterization of NbTiN thin films prepared by reactive DC-magnetron sputtering, *Applied Superconductivity, IEEE Transactions on* **13**, 3284–3287 (2003).

[40] C. Koch, J. Scarbrough, and D. Kroeger, Effects of interstitial oxygen on the superconductivity of niobium, *Phys. Rev. B* **9**, 888–897 (1974).

[41] J. Halbritter, On the oxidation and on the superconductivity of niobium, *Applied Physics A* **43**, 1–28 (1987).

[42] A. Darlinski and J. Halbritter, Angle-resolved XPS studies of oxides at NbN, NbC, and Nb surfaces, *Surface and Interface Analysis* **10**, 223–237 (1987).

[43] P. Joyez, *The single Cooper pair transistor: a macroscopic quantum system*, Ph.D. thesis, Universite Paris 6 (1995).

[44] T. A. Fulton and L. N. Dunkleberger, Lifetime of the zero-voltage state in Josephson tunnel junctions, *Phys. Rev. B* **9**, 4760–4768 (1974).

[45] John Clarke and Frank K. Wilhelm, Superconducting quantum bits, *Nature* **453**, 1031–1042 (2008).

[46] O.-P. Saira, A. Kemppinen, V. F. Maisi, and J. P. Pekola, Vanishing quasiparticle density in a hybrid Al/Cu/Al single-electron transistor, *Phys. Rev. B* **85**, 012504 (2012).

[47] R. Dynes, V. Narayanamurti, and J. Garno, Direct measurement of quasiparticle-lifetime broadening in a strong-coupled superconductor, *Phys. Rev. Lett.* **41**, 1509–1512 (1978).

[48] R. M. Lutchyn, Effect of quantum fluctuations on even-odd energy difference in a Cooper-pair box, *Phys. Rev. B* **75**, 212501 (2007).

[49] N. A. Court, A. J. Ferguson, Roman Lutchyn, and R. G. Clark, Quantitative study of quasiparticle traps using the single-Cooper-pair transistor, *Phys. Rev. B* **77**, 100501 (2008).

[50] Yonatan Dubi, Yigal Meir, and Yshai Avishai, Nature of the superconductor-insulator transi-

tion in disordered superconductors, *Nature* **449**, 876–880 (2007).

[51] Benjamin Sacepe, Thomas Dubouchet, Claude Chapelier, Marc Sanquer, Maoz Ovadia, Dan Shahar, Mikhail Feigel'man, and Lev Ioffe, Localization of preformed Cooper pairs in disordered superconductors, *Nat Phys* **7**, 239–244 (2011).

[52] P. C. J. J. Coumou, E. F. C. Driessen, J. Bueno, C. Chapelier, and T. M. Klapwijk, Electrodynamic response and local tunneling spectroscopy of strongly disordered superconducting tin films, *Phys. Rev. B* **88**, 180505 (2013).

[53] C. Kittel, *Introduction to solid state physics*, 5th ed. (New York: Wiley, 1976).

[54] Michael Tinkham, *Introduction to Superconductivity*, edited by Dover Publications (Dover Publications, 2004).

[55] V. V. Moshchalkov, L. Gielen, C. Strunk, R. Jonckheere, X. Qiu, C. Van Haesendonck, and Y. Bruynseraede, Effect of sample topology on the critical fields of mesoscopic superconductors, *Nature* **373**, 319–322 (1995).

[56] A. K. Geim, I. V. Grigorieva, S. V. Dubonos, J. G. S. Lok, J. C. Maan, A. E. Filippov, and F. M. Peeters, Phase transitions in individual sub-micrometre superconductors, *Nature* **390**, 259–262 (1997).

[57] J. J. Palacios, Vortex matter in superconducting mesoscopic disks: Structure, magnetization, and phase transitions, *Phys. Rev. B* **58**, R5948–R5951 (1998).

[58] Gheorghe Stan, Stuart B. Field, and John M. Martinis, Critical field for complete vortex expulsion from narrow superconducting strips, *Phys. Rev. Lett.* **92**, 097003 (2004).

[59] J. T. Peltonen, J. T. Muhonen, M. Meschke, N. B. Kopnin, and J. P. Pekola, Magnetic-field-induced stabilization of nonequilibrium superconductivity in a normal-metal/insulator/superconductor junction, *Phys. Rev. B* **84**, 220502 (2011).

[60] I. Aranson, M. Gitterman, and B. Ya. Shapiro, Onset of vortices in thin superconducting strips and wires, *Phys. Rev. B* **51**, 3092–3096 (1995).